Journal of the mechanical behavior of biomedical materials 68 (2017) 32–41

Contents lists available at ScienceDirect

Journal of the Mechanical Behavior of Biomedical Materials

journal homepage: www.elsevier.com/locate/jmbbm

Wave propagation in ballistic gelatine

Srinivasan S. Naarayan[1], Ghatu Subhash*

Mechanical and Aerospace Engineering, University of Florida, Gainesville, FL 32611, USA

ARTICLE INFO

Keywords:
Ballistic gelatin
Wave propagation
Mooney-Rivlin model
Neo-Hookean model
Polymer Hopkinson bar
Dynamic response

ABSTRACT

Wave propagation characteristics in long cylindrical specimens of ballistic gelatine have been investigated using a high speed digital camera and hyper elastic constitutive models. The induced transient deformation is modelled with strain rate dependent Mooney-Rivlin parameters which are determined by modelling the stress-strain response of gelatine at a range of strain rates. The varying velocity of wave propagation through the gelatine cylinder is derived as a function of prestress or stretch in the gelatine specimen. A finite element analysis is conducted using the above constitutive model by suitably defining the impulse imparted by the polymer bar into the gelatine specimen. The model results are found to capture the experimentally observed wave propagation characteristics in gelatine effectively.

1. Introduction

Gelatin and gelatin compounds are often used as tissue surrogates in a range of biomedical applications for studying tissue damage and modeling tissue response during reconstructive surgery. Their ability to be molded with customizable properties makes them ideal candidates as surrogates for human organs, tissue, and muscle. Gelatin is also used as a projectile for testing of aircraft windows and engine components to simulate bird impact during flight (Wilbeck and James, 1981). Gelatin is basically a fibrous protein extracted from the skin, bones, organs of animals and even sea weed. Ballistic gelatin, which is popularly used in many dynamic applications, is prepared with collagen extracted from a pig skin. Typically, the preparation is called 'acid preparation' (Type-A) at pH 4.6 and its strength is quoted as 250 Bloom (Jussila, 2004). There are two popular ways of gelatin preparation: (i) NATO Gelatin, in which gelatin and water are mixed in the ratio of 1:4 by volume and (ii) Fackler gelatin where gelatin and water are mixed in the ratio of 1:9 by volume (Jussila, 2005).

Due to their wide range of applications, gelatin has been characterized under both quasi static and dynamic loads. While the quasi static and low-velocity behavior has been described through hyperelastic models (Cronin and Falzon, 2009; Liu et al., 2013; Ravikumar et al., 2015), the high-velocity material behavior was described through hydrodynamic theory (Airoldi and Cacchione, 2006; Johnson and Holzapfel, 2003; Shepherd et al., 2009; Wightman et al., 2010; Heimbs, 2011; Appleby Thomas et al., 2011; Toyoda and Gupta, 2014). Low-velocity tests (< 30 m/s) on gelatin have been conducted in drop tower equipment (Cronin and Falzon, 2009; Naarayan et al., 2015) or split Hopkinson pressure bar (Cronin and Falzon, 2011; Subhash et al., 2012; Chen et al., 1999; Liu and Subhash, 2006). Salisbury and Cronin (2009) and Kwon and Subhash (2010) conducted high deformation rate characterization of ballistic gelatin at nominal strain rates up to 4,000/s using a polymer split Hopkinson bar. Richler and Rittel (2014) used a metallic SHPB and developed empirical models to fit the experimental data. Cronin and Falzon (2009) and Ravikumar et al., (2015) used a hyper viscoelastic constitutive model to describe the behaviour of gelatin in the quasistatic and intermediate strain rate regimes. An Ogden type strain energy density function was employed for the elastic component and a single Prony exponential term was used to capture the observed rate-dependent response over multiple strain rates. Liu et al. (2005) conducted uniaxial compression and simple shearing experiments on gelatin and determined the moduli in Mooney-Rivlin model to describe the elastic behavior at low strain rates.

Gelatin has also been used as a tissue surrogate for understanding the deformation behaviour of human organs under shock loading or ballistic impact (Shepherd et al., 2009; Appleby-Thomas et al., 2011). Wen et al., (2013) investigated cavity formation when gelatin is subjected to high velocity impact. Song and Chen (2004) studied non-uniform deformation of soft gels at low velocities to determine the material properties. Despite the variety of experimental studies reported here, the literature on non-uniform behavior and wave propagation characteristics in gelatin are limited.

In this work, the wave propagation behavior in ballistic gelatin is investigated by imparting an impulse motion into a long cylindrical gelatin specimen and then capturing the transient deformation using a

* Corresponding author.
E-mail address: subhash@ufl.edu (G. Subhash).
[1] Present/permanent address: Structural Technologies Division, National Aerospace Laboratories, Kodihalli, Bangalore 560017, India.

http://dx.doi.org/10.1016/j.jmbbm.2017.01.030
Received 10 October 2016; Received in revised form 19 January 2017; Accepted 23 January 2017
Available online 23 January 2017

high speed digital camera. To model this response, the high strain rate behavior of gelatin is determined at a range of strain rates using a polymer split Hopkinson pressure bar (PSHPB). A hyperelastic Mooney-Rivlin model is then employed to capture the constitutive response. This model is applied to wave propagation in a long cylindrical specimen. To further understand the behavior observed in the experiments, the variation of the wave velocity with stretch is explained in terms of two Mooney-Rivlin constants. The equivalent Neo-Hookean model (with only a single constant) is then defined. Using these model parameters, finite element analysis of the wave propagation in the gelatin cylinder was conducted by explicitly defining the momentum transfer from the loading device to the geletin. The resulting wave propagation characteristics are then compared to the experimental observations.

2. Experimental details

2.1. Preparation of the gelatin test specimens

Gelatin powder was purchased from Vyse-Gelatin Innovations, Schiller Park, IL, USA. The gelatin solution with 250 bloom strength was prepared as described in Kwon and Subhash (2010). The procedure involved mixing 2g of gelatin powder with 4g of filtered water at 25° C. A drop of defoamer along with 14g of hot water (at 60 °C) was then added to the mixture and the entire mixture was stirred at regular intervals of 3min for 15s each until the powder is fully dissolved. The mixture was then poured into plastic moulds and placed in a refrigerator for 2h at 5° C and the experiments were conducted within 1 minute after they were taken out of the refrigerator. No calibration of the gelatine was performed as the intent was to study wave propagation behaviour in long cylindrical specimens utilizing a self-consistent approach based on the experimentally determined constitutive properties from the small gelatin samples regardless of how they are made and as long as they exhibit hyperelastic behavior.

Two types of test specimen were prepared: (i) long cylinders of 19mm diameter and 40mm length for investigation of wave propagation behavior and (ii) thin cylindrical disks of 12.7mm diameter and 2mm thickness for determining the constitutive response at high strain rates. The prepared specimens were stored in a refrigerator for 2 hours at 5°C and tests were conducted in ambient conditions at room temperature within 1 minute after they were taken out of the refrigerator.

2.2. Wave propagation in gelatin cylinders

Cylindrical specimens were placed in a polymer (acrylic) split Hopkinson pressure bar (PSHPB) and subjected to impulse load of duration of roughly 0.33ms. The principle of application of impulse load to gelatin by the PSHPB is briefly discussed here. The PSHPB consists of a striker bar, an incident bar and a transmission bar, all of diameter 25.4mm (Kwon and Subhash, 2010; Liu and Subhash, 2006). The specimen is placed between the incident and the transmission bars. The striker bar is launched from a gas gun towards the incident bar at predetermined velocity. The impact generates a stress pulse in the incident bar and travels towards the specimen. The duration of the stress pulse is equal to the round trip travel time of the longitudinal wave in the striker bar. When the stress wave in the incident bar reaches the bar-specimen interface, the rapid motion of the incident bar imparts an impulse into the gelatine and generates a stress wave within the cylindrical specimen. The associated temporal and spatial deformation of gelatine is captured by a high speed camera at 14,000 frames per second. Note that due to the low wave velocity in the gelatin, it takes several milliseconds for the stress wave to traverse the length of the long cylindrical specimen and hence, the transmission bar acts only as a rigid support during this time interval. The transient deformation of the specimen during this time interval is of interest in this study. A schematic of the test setup is shown in Fig. 1. Three specimens were tested at each incident bar velocity of approximately 1.7 m/s, 2.1 m/s, and 3.6 m/s to ensure repeatability of the behaviour.

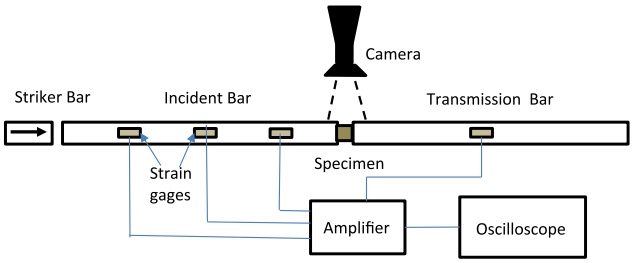

Fig. 1. Experimental setup for testing of gelatin specimens to study wave propagation in polymer split Hopkinson pressure bar.

2.3. High strain rate stress-strain testing of gelatin using PSHPB

Due to the low-impedance (product of density, wave velocity, and area of cross section) of gelatin, traditional metallic SHPB has been shown to be unsuitable for extracting its constitutive response (Liu and Subhash, 2006). Therefore, alternate methods such as hollow transmission bar and PSHPB have been used effectively in the literature (Cronin and Falzon, 2009; Salisbury and Cronin, 2009; Liu and Subhash, 2006; Cronin and Falzon, 2011; Wen et al., 2013). In both cases the aim is to reduce impedance of the bar close to that of the soft specimen, yet ensuring that the bar stiffness and strength are sufficiently high to keep the testing equipment relatively rigid during the deformation of the soft specimen. A schematic of the test setup is shown in Fig. 1. The thin gelatin specimen is again sandwiched between the transmission and incident bars. Similar to previous tests on long cylindrical specimens, the stress wave reaches the specimen, except that now it deforms the specimen uniformly because the incident stress pulse duration is significantly greater than several times the time required for stress wave to travel through the specimen thickness. A portion of the wave is transmitted to the transmission bar and the rest is reflected back into the incident bar. The amplitude of the reflected wave is proportional to the strain rate in the specimen and that of the transmitted wave is related to stress in the specimen. However, the traditional equations used for metallic SHPB need to be modified to account for the viscoelastic nature of the polymer bars. The specific procedure for extracting the stress-strain response for soft materials using a PSHPB involves many steps and is well-documented in Liu and Subhash (2006) and Liu et al. (2005). The viscoelastic wave propagation in the polymer bar results in dispersion and attenuation of wave signals as they travel along the bars. To capture this phenomenon, three strain gages were bonded on the incident bar and one gage at the center of the transmission bar length. The wave signals captured by these strain gages reveal the severity of dispersion and attenuation in the propagating waves. Utilizing any two of these three signals (e.g., strain gages 1 and 3 in Fig. 1) on the incident bar and an iterative procedure developed by Liu et al. (2005), the viscoelastic behavior of the polymer bars can be fully characterized in terms of an impulse response function (IRF) which allows one to predict the shape of the stress pulse at any position in the bar for any instant of time. By reconstructing the incident and reflected signals at the gage locations, the stress-strain response in the specimen can be determined using the following equations (Kwon and Subhash, 2010; Liu and Subhash, 2006)

$$\sigma_s(t) = \frac{A_b}{A_s}\int_0^t E_b(t-\tau)\frac{\partial \varepsilon_t}{\partial \tau}d\tau \quad (1)$$

$$\varepsilon_s(t) = \frac{2}{l_s}\int_0^t C(0)\varepsilon_r(\tau)d\tau \quad (2)$$

Where ε_r and ε_t are the time varying reflected and transmitted strains,

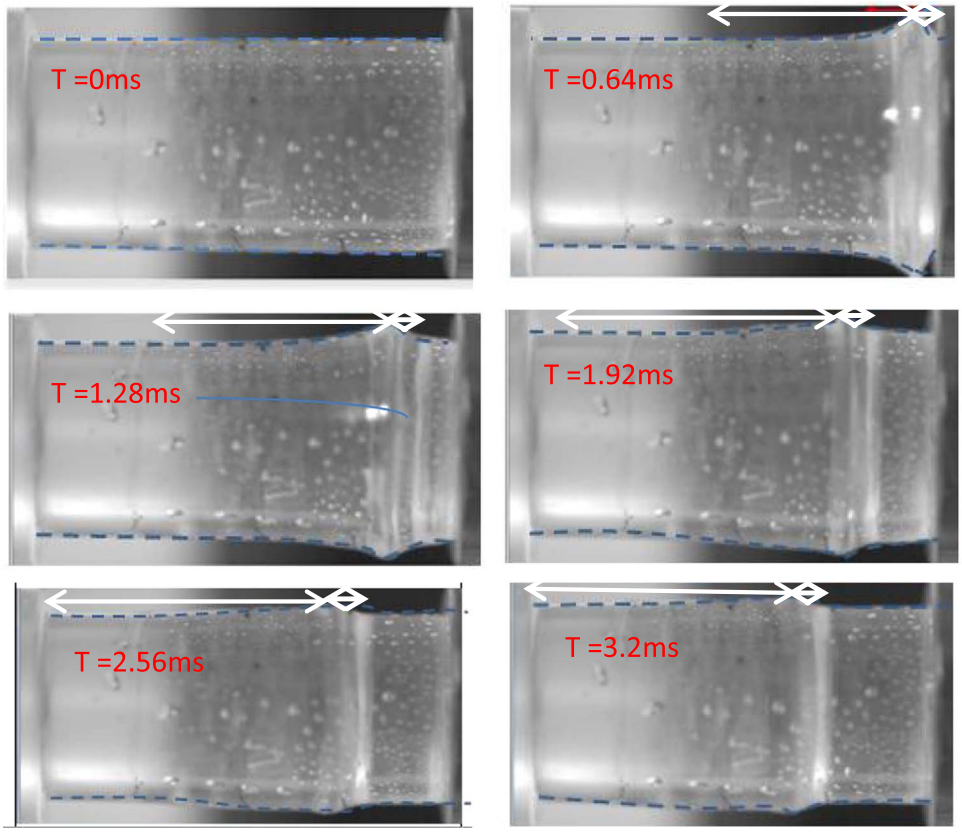

Fig. 2. Images of wave propagation in a cylindrical ballistic gelatin specimen subjected to an impulse load in a polymer split Hopkinson pressure bar.

respectively, l_s is the original length of the specimen, and A_b and A_s are cross sectional areas of bar and specimen, respectively. C is wave velocity in the bar given by $C(t)=\frac{E_b(t)}{\rho C(0)}$ where $E_b(t)$ is the stress relaxation modulus function of the bar and ρ is the density of gelatin. The wave velocity in undeformed material is calculated as discussed in Liu and Subhash (2010), given by $C(0) = \sqrt{(E_i/\rho)}$, where E_i are the visco-elastic elements that approximate the modulus of the bar and ρ is density. Using the above equations the stress-strain response of gelatin at a range of strain rates is determined (Kwon and Subhash, 2010). The derivation of the expression in Eq. (2) and of the expression for C(t) is given in Section 5.

The low impedance of gelatin necessitates small specimen thickness to satisfy stress equilibrium (Kwon and Subhash, 2010; Liu and Subhash, 2006; Song and Chen, 2004 and 2005) and obtain reliable stress-strain response at high strain rate. Subhash and Ravichandran (2000) established minimum thickness requirements of a specimen based on specified number of wave reflections for stress equilibration. They suggested that at least four round-trip travel times are necessary within a specimen to achieve the dynamic stress equilibrium. Song and Chen (2004) validated this method for soft specimens by using quartz gages on both sides of a soft specimen and comparing the signals to establish stress equilibrium. Utilizing the same approach, Kwon and Subhash (2010) determined that a 2 mm thickness is sufficient to ensure dynamic stress equilibrium in PSHPB testing. Based on these considerations a gelatin sample of 2 mm thickness and 12.7 mm diameter was used for determination of stress-strain response.

An important consideration while testing soft materials at high strain rates is radial inertial effect which a material point experiences due to sudden radial acceleration during uniaxial compression of the specimen. In uniaxial compression the material points on the outer surface are free to move radially and hence experience high radial accelerations and thereby exert an inertial force or stress on the material within the cylinder. This inertial stress is therefore maximum at the central region of the specimen due to confinement. While this inertial stress magnitude may be only on the order of hundred mega pascals or less (Song and Chen, 2004 and 2005), it is a significant fraction of the strength of the soft material. On the other hand, this stress magnitude is negligible in metallic or ceramic materials in comparison to their failure strength (Warren and Forrestal, 2010). In addition, the dynamic loading causes large radial displacement in a soft material during the experiment. The above discussed inertia related issues cause additional stiffness in the material. The dependence of radial inertial stress on strain ε_x, strain rate $\dot{\varepsilon}_x$and strain acceleration $\ddot{\varepsilon}_x$is expressed as hydrostatic pressure p given by (Warren and Forrestal, 2010)

$$p = \frac{\rho}{4(1-\varepsilon_x)^2}\left[\frac{3(\dot{\varepsilon}_x)^2}{2(1-\varepsilon_x)}+\ddot{\varepsilon}_x\right](a_0^2-r^2) \tag{3}$$

where, ρ is density, r is the radial distance of a material point and a_O is the outer radius of the specimen. Note that the pressure varies with square of the radial distance r and is maximum at the centre of the specimen and reduces in a parabolic fashion to zero at the outer radius of the specimen. As a result, the average additional pressure $\bar{p}$ which would be measured in the experiment along with the axial stress is calculated (Warren and Forrestal, 2010) as

$$\bar{p}=\frac{3\rho a_0{}^2}{16(1-\varepsilon_x)^3}(\dot{\varepsilon_x})^2+\frac{\rho a_0^2}{8(1-\varepsilon_x)^2}\ddot{\varepsilon_x} \tag{4}$$

This additional stress should be subtracted from the measured axial stress in the transmitted bar as this stress doesn't contribute to the deformation of the material. More details of this procedure are given in Nishida (2010) and Nishida and Chen (2010).

3. Experimental results

3.1. Wave propagation in cylindrical specimens

Fig. 2 shows a sequence of high speed images of gelatin deformation in a 40mm long cylindrical specimen due to an impulse loading in a PSHPB where the incident bar velocity was measured at 3.49 m/s. The six images are sequenced at 640 microseconds apart with the last image at 3200 microseconds. Fig. 2(a) shows the initial state of the sample. After imparting impulse into the gelatine specimen, the motion of the incident bar ceases at 640 microseconds (Fig. 2(b)) and resumes after 3200 microseconds when the reflected wave from the specimen in the incident bar reaches the impact end and then arrives back again to this interface causing a second impulse loading on the gel specimen. This interval allows for observation of the wave motion and the associated gel deformation over 3200 μs.

Upon receiving an impulse load by the incident bar in PSHPB, a longitudinal stress wave is generated in gelatine and propagates along the length of the specimen. The sequence of images shown in Fig. 2(b)-(f) illustrate gel deformation as the wave propagates. Upon impact, the generated wave causes a bulge in the specimen (T=0.64 ms) where the transverse strain is maximum. This bulge tapers down to the original diameter of the cylinder on both the front and the rear of the wave crest as shown by the blue dashed boundary lines. The white arrows above the specimen indicate the length over which the deformation extends in the specimen. The taper ahead of the bulge extends over a longer distance than the one behind the crest. This observation indicates that the wave-front travels at a higher speed than the point at the crest of the wave. With time, the amplitude of the crest attenuates and disperses as it propagates along the length of the cylindrical specimen. In Fig. 2(f) the wave-front almost reaches the end of the specimen even though the wave-crest has only travelled $1/3^{rd}$ of the specimen length. The taper length at the back of the wave-crest remains almost the same with time. The profiles of the wave at various time intervals are superposed in Fig. 3 to reveal the dispersion, peak attenuation, and positions of wave-front and wave-crest with time.

The variation in velocities of the wave-front and wave-crest for three different bar-input velocities are shown in Fig. 4. It is seen that both these velocities increase with increasing incident bar velocity. However, the wave-front velocity reveals a sharp drop within 250 μs, indicating that the initial velocity of the wave is influenced by the bar impulse velocity and once this influence is diminished, the wave-front travels at its characteristic velocity which depends on the stretch of the material as will be shown in the next section. On the other hand, the wave-crest velocity gradually decreases as it propagates along the length of the cylinder. Due to its gradual attenuation, it cannot be tracked in the images once its amplitude falls close to the original diameter of the cylinder. Regardless, the wave velocities vary with incident bar velocity and this can be explained based on the prestress induced in the specimen as discussed in the next section.

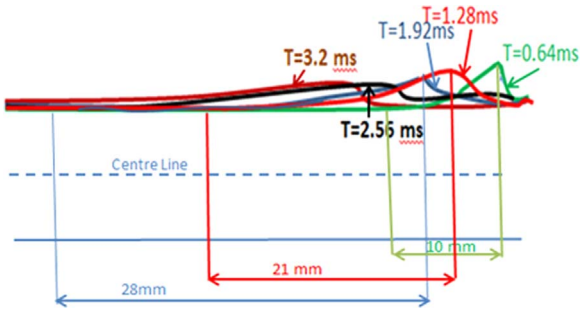

Fig. 3. Profiles of the wave in gelatin specimen at various time intervals revealing crest attenuation and dispersion as it traverses the specimen length.

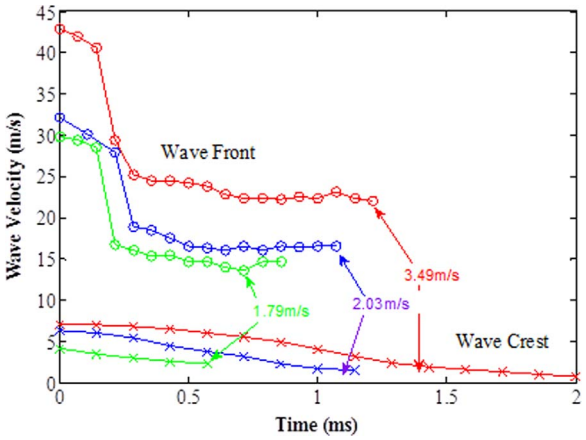

Fig. 4. Variation of the velocities of propagation of the wave-crest and wave-front with time for different incident bar velocities.

4. Constitutive modeling

The intent of the modelling effort is to first capture the constitutive behavior using the well-established hyper-elastic models and determine the relevant constants. In the next phase, we will apply these models to capture the wave propagation behavior in gelatine cylinder. In literature both Neo-Hookean and Mooney-Rivlin models have been used. While the former uses a single constant in its constitutive equation, the latter is more versatile as it utilizes two constants to capture the complex behaviour of gels. In these models, the strain energy function W is given by

$$W = K(I_1-3) \quad \rightarrow \text{Neo} - \text{Hooken(NH) model} \tag{5}$$

$$\textit{and } W = C_1(I_1-3)+C_2(I_2-3) \quad \rightarrow \text{Mooney} - \text{Rivlin(MR) model} \tag{6}$$

Where K, C_1 and C_2 are constants and I_1 and I_2 are the stress invariants of Cauchy-Green tensor. The Mooney-Rivlin model, Eq. (6), can be rewritten in terms of the principal stretches λ_1, λ_2 and λ_3 (Treloar, 1975) as

$$W = C_1(\lambda_1^2+\lambda_2^2+\lambda_3^2-3)+C_2\left(\frac{1}{\lambda_1^2}+\frac{1}{\lambda_2^2}+\frac{1}{\lambda_3^2}-3\right). \tag{7}$$

Consider a uniaxial test on an isotropic cylindrical specimen where the load is applied in x_1-direction yielding an extension ratio or compression ratio $\lambda_1=\lambda$. The condition of isotropy in the other two directions yields $\lambda_2=\lambda_3$. Applying the incompressibility condition ($\lambda_1\lambda_2\lambda_3=1$) for an isotropic material, we obtain $\lambda_2=\lambda_3=\frac{1}{\sqrt{\lambda}}$. The above strain energy functional for MR model can now be written in terms of stretch λ as

$$W = C_1\left(\lambda^2+\frac{2}{\lambda}-3\right) + C_2\left(2\lambda+\frac{1}{\lambda^2}-3\right) \tag{8}$$

The first Piola-Kirchoff elastic stress can be obtained by differentiating the energy function with stretch, i.e.,$\sigma_{el}=\frac{\partial W}{\partial \lambda}$, in terms of C_1 and C_2 (Kobayashi and Vanderby1, 2005)

$$\frac{\sigma_{el}}{2(\lambda-\frac{1}{\lambda^2})} = C_1 + \frac{C_2}{\lambda} \tag{9}$$

Thus, the stress in the gelatin cylinder can be fully expressed in terms of the MR constants and the stretch of the material. However, as described previously, the behaviour of hyperelastic materials also depends on the prestress (or prestrain) in the material (Kobayashi and Vanderby1, 2005) which can influence the wave behaviour observed in Fig. 4 where the velocities of wave-front and wave-crest increase with increasing incident bar velocity. These phenomena can be explained through the change in prestress (or prestrain) in the material as the wave propagates in the sample (see Fig. 2). Considering wave

propagation only in x_1-direction with a prestress T as the Cauchy stress applied by the incident bar, the equations of motion can be written (Kobayashi and Vanderby1, 2005).

$$(\widetilde{C}_{11}+T)\frac{\partial^2 u_1}{\partial x^2} = \rho\frac{\partial^2 u_1}{\partial t^2} \tag{10}$$

Where $\widetilde{C}_{11}$is the stiffness and the Cauchy stress T causes a stretch of λ in x_1-direction through the relation

$$T = \lambda\frac{\partial W}{\partial \lambda} \tag{11}$$

Note that the term $(\widetilde{C}_{11}+T)$ is the effective stiffness in the presence of pre-stress. The dilatational velocity in the x_1-direction is now given by

$$v = \sqrt{\frac{\widetilde{C}_{11} + \quad T}{\rho}} \tag{12}$$

Where $\widetilde{C}_{11}$ can be derived in terms of the deformation gradient $F_{11}=\frac{\partial x_1}{\partial X_1}=\lambda$ as (Kobayashi and Vanderby1, 2005) as

$$\widetilde{C}_{11} = \frac{1}{\det\ (F)}(F_{11})^4\frac{\partial^2 W}{\partial E^2_{11}} \tag{13}$$

For an incompressible material det(F)=1. The finite Green strain tensor ε_{11} is given in terms of the deformation gradient as

$$\varepsilon_{11} = \frac{1}{2}(\lambda^2-1) \tag{14}$$

Utilizing Eqs. (8), (13) and (14) we can derive the expression for the numerator of Eq.(12) as

$$\widetilde{C}_{11} + T = \left(2\lambda^2+\frac{4}{\lambda}\right)C_1+\left(\frac{6}{\lambda^2}\right)C_2 \tag{15}$$

The above equation illustrates that the wave velocity in gelatine depends on the stretch ratio λ (which is nothing but prestrain). It would be of interest to know the value of $\widetilde{C}_{11}$ at zero strain (λ=1) from Eq. (15) which for MR model is given by

$$\widetilde{C}_{11}(1) + T(1)_{MR} = 6[(C_1 + C_2)]_{MR} \tag{16}$$

For comparison purposes, if we model the gel behavior as a Neo-Hookean (NH) material (i.e., C_2=0), we reduce Eq. (6) to Eq. (5) and hence we can write Eq. (16) as

$$[\widetilde{C}_{11}(1) + T(1)]_{NH} = 6K \tag{17}$$

Now we can plot the wave velocity as a function of prestrain λ. But the constants C_1 and C_2 are unknown which may depend on strain rate of the material. Recall that gelatine is highly rate sensitive material (Kwon and Subhash, 2010) and the local strain rate in the wave propagation experiment changes not only spatially and temporally, but also with initial velocity of the indent bar (see Figs. 2–4). Therefore, we will first obtain stress-strain response experimentally at a range of strain rates and try to evaluate the constants used in the relations above.

4.1. Stress-strain response of gelatine

Fig. 5 shows true stress (λ*Engineering stress) and true strain (-ln(λ)) curves at a range of strain rates from 0.0107/s-6600/s. These curves are corrected for radial inertial stress as described earlier (Nishida, 2010; Nishida and Chen, 2010). These curves appear slightly different from Kwon and Subhash (2010) because such correction for radial inertia was not applied in that article. Without this correction, the curves display a plateau in the initial strain range due to slight non-equilibrium in the early stages of deformation which vanishes when equilibrium gets established later (Song and Chen, 2004). The reported curves in Fig. 5 also are slightly different from those of Richler and Rittel (2014) and Salisbury and Cronin (2009) for similar strain rates due to differences in mixing methods, temperature, and inhomogeneities (small bubbles, cracks, and fissures) present in the virgin specimens which may give lower stiffness in their early response. In addition, Richler and Rittel (2014) used a metallic Hopkinson bar and they noted no stress increase even at a strain of 0.2, probably due to high low-signal to noise ratio which may have made identification of stress increase difficult. We have also noted that Richler and Rittel (2014) have used a gelatine density of 1000 g/cm^3 which is not appropriate. All these differences could have caused discrepancies in reported literature values.

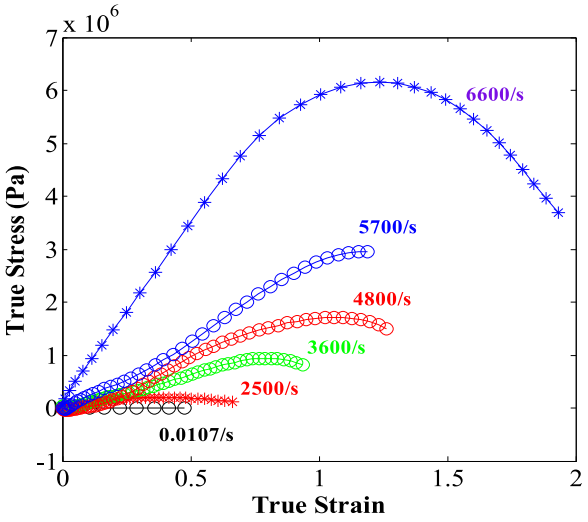

Fig. 5. True stress-strain curves at different strain rates for ballistic gelatin.

In Fig. 5, the strain rate dependence of stiffness and strength is clearly observed. The curves show an increasing stress with strain until the stress reaches a peak and then decrease for large strain values. This trend is very clear for the highest strain rate (6600/s). The curves at other strain rates clearly show a peak but the decreasing trend is not observed since the load or true stress didn't go beyond the peak. Similar trend for decreasing true stress is also observed by other researchers (Richler and Rittel, 2014).

Now consider Eq. (9) and plot $\boldsymbol{\sigma}_{el}/(2*(\lambda-1/\lambda^2))$ as the ordinate and $1/\lambda$ as the abscissa for various values of $\boldsymbol{\sigma}_{el}$ and λ. Utilizing a polyfit command with degree one, we can now determine the constants C_1 and C_2 based on least square criterion. With these values of Mooney-Rivlin constants, the stress-strain curves are generated by evaluating the true stress expression in Eq. (11) using Eq. (9). Fig. 6 compares the experimental and model true stress-strain curves which reveal that

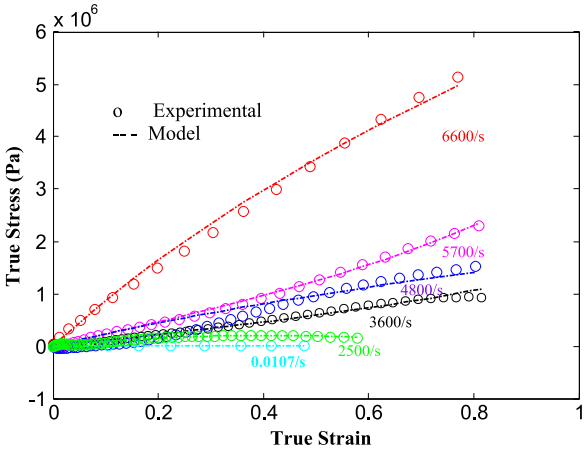

Fig. 6. Comparison of the experimental and MR model true stress-strain curves in compression.

Table 1
Mooney-Rivlin constants obtained from curve-fit to the experimental data.

Strain rate (s^{-1})	$C_1(N/m^2)$	$C_2(N/m^2)$	$6(C_1+C_2)$ (N/m^2)	True strain range
0.0107	$4.0482x10^3$	$-1.1569x10^3$	$1.7348x10^4$	0.47
2500	$3.42x10^5$	$-1.652x10^5$	$1.06x10^6$	0.60
3600	$1.322x10^5$	$0.595x10^5$	$1.15x10^6$	0.81
4800	$2.90x10^5$	$0.087x10^5$	$1.792x10^6$	0.81
5700	$2.7x10^5$	$1.32x10^5$	$2.41x10^6$	0.81
6600	$1.23x10^6$	$-0.135x10^6$	$6.57x10^6$	0.81

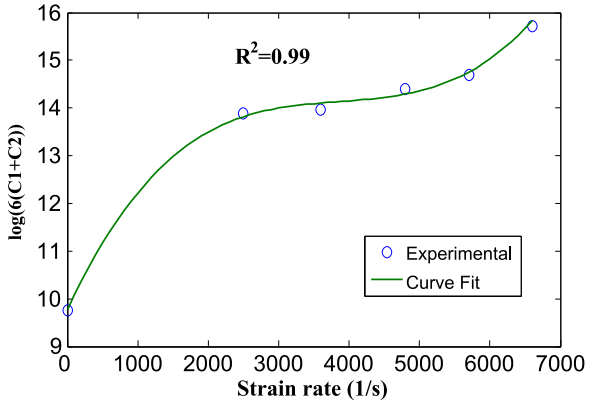

Fig. 7. Plot of variation of the term $6(C_1+C_2)$ with strain rate.

the above values of constants capture the stress-strain response up to a true strain as large as 0.8. The values of the constants C_1 and C_2 and their range of validity are shown in Table 1. Some values of constants are negative and will influence the model behavior in a complex way. Also shown in Table 1 are the values of the term $6(C_1+C_2)$ in Eq. (16) which signifies the stiffness in the presence of prestress. From Eqs. (12) and (15) it is seen that the wave velocity in gelatine is dependent on both the Mooney-Rivlin constants, and that the wave velocity at zero strain ($\lambda=1$) is dependent on sum of the constants ($6(C_1+C_2)$). This term is plotted as a function of strain rate in Fig. 7 which reveals that it increases (and hence the wave velocity) with strain rate in a nonlinear fashion. The third order polynomial model fit is also shown in the Figure. It is to be noted that Richler and Rittel (2014), based on empirical evidence, have derived a linear relationship between the logarithm of stress and strain rate for ballistic gelatin. The current work reveals that the relationship between the logarithm of the sum of the Mooney-Rivlin constants (the sum of the constants is directly proportional to the stress) and the strain rate is much more complex. It is seen from Fig. 7 that a third order polynomial instead of a linear fit describes the relationship between strain rate and the logarithm of Mooney-Rivlin constants appropriately. Also the current work presents finite strain hyperelastic models such as the Mooney-Rivlin and Neo-Hookean models which can model the complex phenomena observed in gels. Recall that a completely incompressible material cannot support elastic waves nor the wave deformation observed in the test. Also, the pressure effects such as radial inertial effects which occur during rapid loading will not be observed in fully incompressible material. Most of the commercial finite element packages make the assumption of near incompressibility at large strains. In our study we have used a nearly incompressible Mooney Rivlin material model with Poisson's ratio of 0.49 was used. Even though the Mooney-Rivlin and Neo-Hookean models are not strain rate dependent, the data from this work provides a relationship between the constants and strain rate which will be useful when the average strain rate of loading is known as will be demonstrated later where the phenomena observed in Fig. 2 are modelled using the average strain rate of loading. With the values of constants shown in Fig. 7 we will now try to simulate the wave propagation behaviour in gelatin.

Despite the trend shown in Fig. 7, it is not possible to separately determine the values of constants C_1 and C_2 in this procedure as they depend on strain rate. Since the prime goal of this analysis is to model the wave propagation behavior observed in Fig. 2, knowledge of the sum of the constants alone would be of limited use. To overcome this limitation, we will use the single constant NH model that is equivalent to the derived two constant MR model. The equivalence is based on the wave velocity in the gelatine (which is a function of stretch) by defining the NH model with the constant $K = (C_1+C_2)$ such that it will result in the same initial wave velocity at zero strain (i.e., $\lambda=1$) for both the models. The process is described in the following paragraph.

In the previous analysis on the stress-strain curves, we used MR model because of its versatility in capturing the response with two constants. If we had used the NH model it would have only captured the average response due to the single constant in the model. Also recall from Table 1 that some of the values of C_2 constant are negative suggesting that the stress does not rise consistently at all strain rates. Therefore the initial wave velocity of the MR model is equated to that of the NH model by considering the stiffness at zero strain. To check the validity of this approach the true stress-strain curves for both the models are plotted in Fig. 8 for the selected strain rates. It is evident that for low strain values up to 0.59 the equivalent Neo-Hookean model compares well with the Mooney-Rivlin model at all the strain rates considered. Since the strain observed in the experiments in Fig. 2 is well within this range (to be discussed in Section 5) and the strain rates are also in the lower range as will be discussed later, the Neo-Hookean model should be adequate to capture the wave propagation phenomenon well.

It is evident from Figs. 2–4 that not only the velocities of the wave-crest and wave-front vary with time but also the strain in the wave-crest varies as it propagates. So it would be of interest to study, using the equations derived above, how the wave velocity varies with prestress/prestrain which is caused solely by the dynamic compressive loading imparted by the PSHPB. The variation of the wave velocity with static compressive pre strain for the newly constructed NH model is shown in Fig. 9. There are many observations that can be made from this figure: (i) as expected, for static loading (strain rate of 0.0107/s), the wave velocity is not dependent on prestrain and is almost constant (zero); (ii) for dynamic strain rates, the wave velocity not only increases with strain rate but also with pre strain in a non-linear way, and (iii) the rate of increase in wave velocity with pre strain increases rapidly with strain rate, especially at higher strain rates. Clearly, the wave velocity increases with compressive prestrain for a given strain rate in a complex way. With this model behavior we will now embark on

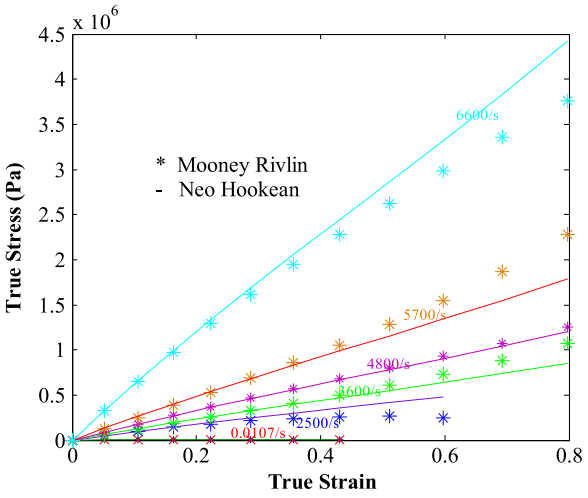

Fig. 8. Comparison of stress-strain curves between the Mooney-Rivlin and the equivalent Neo-Hookean Models.

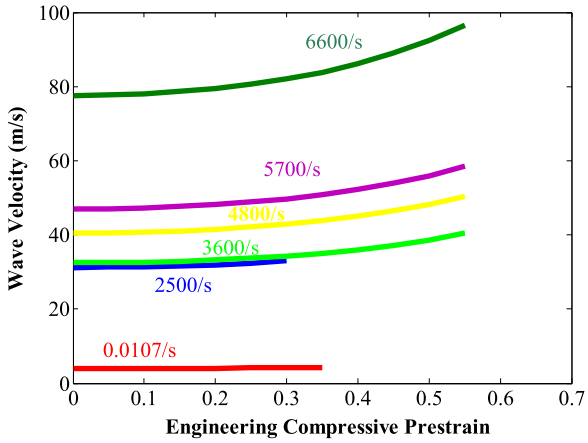

Fig. 9. Variation of dilatational wave velocity with stretch at various strain rates using the equivalent Mooney-Rivlin Model.

capturing the wave propagation characteristics in the gelatine cylinders.

5. Modeling the gelatin deformation during wave propagation

To model the wave propagation phenomenon in a cylindrical specimen, analytical expressions were derived for the interaction between the gelatin surface and the incident bar. These equations were implemented in LS-DYNA software by constructing a finite element model of the full cylindrical specimen and imparting appropriate loading and boundary conditions. A total of 9949 constant-stress 8-node solid elements were used to model the 40-mm long cylindrical specimen as shown in Fig. 10. The nodes along the left boundary of the specimen were constrained in x-direction and those at the right-end were given mass for imparting acceleration $a_x(t)$, or body force, in x-direction by the incident bar. As would be seen in subsequent paragraphs that the value of mass at the nodes depend on the time-step required to obtain finer details of deformation. The convergence of the solution for the mesh size was verified by meshing the specimen domain with a range of element aspect ratios.

Assuming linear elasticity, the interaction stress of the incident bar with the gelatine sample can be written as

$$\sigma = \rho c v_t \tag{18}$$

Where ρ is the density of the bar, c is the wave velocity in the bar and v_t is the velocity of the particle in the incident bar interacting with the specimen. The above equation can be rewritten as

$$\sigma = (\rho c dt)\, v_t/dt \tag{19}$$

which can be interpreted as the inertial force of a mass (ρcdt) undergoing an acceleration of v_t/dt on a unit cross sectional area (Timoshenko and Goodier, 1970). v_t can be viewed as the difference in particle velocities of the incident and reflected wave velocities at the incident bar-specimen interface (i.e., $v_t = v_i - v_r$), i.e.,

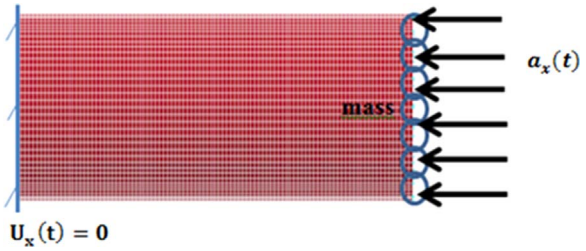

Fig. 10. Specimen discretization and loading conditions.

$$v_t = 2v_i - (v_i + v_r) \tag{20}$$

where $2v_i$ would be the velocity of the particle of mass ρcdt of the incident bar when it initially interacts with a completely stress-free surface of the specimen and $v_i+v_r = v_{int}$ is the velocity with which this interface moves after encountering resistance from the specimen which is undergoing deformation during the experiment in time duration of dt. Similarly, the interfacial force F on a bar of cross-sectional area A can be written as

$$F_{int} = (\rho A c dt)\frac{v_t}{dt} = \rho A c dt\frac{2v_i}{dt} - \rho A c dt\frac{v_{int}}{dt} \tag{21}$$

The differential (ΔF_{int}) of the above equation can be considered as the equation of motion of the interface in terms of the input acceleration($\frac{d(2v_i)}{dt}$) given by

$$\Delta F_{int} = \rho A c dt\frac{d(2v_i)}{dt} - \rho A c dt\frac{dv_{int}}{dt} \tag{22}$$

Eq. (22) can be rearranged in a convenient form as

$$\rho A c dt\frac{dv_{int}}{dt} + \Delta F_{int} = \rho A c dt\frac{d(2v_i)}{dt} \tag{23}$$

where, the right hand side is similar to the body force for the interface which is the input for the nodes in the finite element analysis. This approach is similar to body force equivalent for seismic radiation in literature (Burridge and Knopoff, 1964). However, realize that the above equation of motion is for a purely elastic material. Since the split Hopkinson bar is made of a viscoelastic material, modifications must be made to the above method where the wave velocity at time t is considered as C(t) and the stress is given by

$$\sigma(t) = \int_0^t \rho C(t-\tau) dv_t(\tau) \tag{24}$$

multiplying and dividing the right hand side with C(0), the wave velocity at initial time, Eq. (24) is rewritten as

$$\sigma(t) = \int_0^t \rho C(t-\tau) C(0)\frac{dv_t(\tau)}{c(0)} \tag{25}$$

Considering $d\varepsilon(\tau)=dv_t(\tau)/C(0)$ and comparing this expression with the expression of stress in a viscoelastic material (Eq. (1)), we get

$$E_b(t) = \rho C(t) C(0) \tag{26}$$

and

$$dv_t(t) = C(0) d\varepsilon(t) \tag{27}$$

The expression in Eq. (2) can therefore be easily derived from Eq. (27) since the strain from the SHPB theory which defines the strain in the material at any time as twice the integral of reflected wave velocity with time divided by the length of the sample. From Eq. (22), for a linear elastic material, it is apparent that a constant acting mass of ρAcdt causes stress in the adjoining material with a velocity change of v_t in time dt, where dt can conveniently be chosen as the sampling rate or the time step of analysis, provided that the inputs for the analysis (e.g., displacement, velocity or acceleration) for the active mass (ρAcdt) are given at the same time difference dt. In Eq. (25), for a viscoelastic material, it is observed that the active mass changes with time. So the equations of motion for elastic solid as seen in Eqs.(22) and (23) have to be rewritten to accommodate for the changing mass of the viscoelastic bar as follows

$$\int_0^t \rho A dt C(t-\tau) d\left(\frac{dv_{int}(\tau)}{d\tau}\right) + \Delta F_{int} = \int_0^t \rho A dt C(t-\tau) d\left(\frac{d(2v_i(\tau))}{d\tau}\right) \tag{28}$$

Which can be written in terms of the incident strain $\varepsilon_{i=}v_i/C(0)$ and interfacial strain $\varepsilon_{int}=v_{int}/C(0)$ as

$$\int_0^t A dt E_b(t-\tau) d\left(\frac{d\varepsilon_{int}(\tau)}{d\tau}\right) + \Delta F_{int} = \int_0^t A dt E_b(t-\tau) d\left(\frac{d(2\varepsilon_i(\tau))}{d\tau}\right) \tag{29}$$

Note that the mass appears both in body force term on the right and the inertial force on the left in Eqs. (28) and (29). So an averaging procedure was adopted to decide the mass of the nodes on which the body force or acceleration is imposed. The mass for each time t is found by evaluating the convolution integral in the right hand part of equations and dividing it by the body force term ($\frac{d(2v_i(t))}{dt}$) and then averaging all the masses over time t to arrive at the mass of the interacting element. Dividing this mass by the total number of contact nodes in the specimen surface with the bar gives the mass for each mass element.

The equivalent Neo-Hookean model with constant evaluated using Fig. 7 for strain rate dependence was used for the analysis. The equivalent Neo-Hookean model constant K for the test discussed in Figs. 2 and 3 (strain rate of 600/s, Vo=3.49m/s) is $1.49\text{x}10^4$ N/m^2. To perform the finite element analysis, the NH constant K has to be obtained at the specified strain rate in the experiment from Fig. 7 and the video images. The time required to form the forward taper length just before the wave is initiated is measured from video images. Assuming incompressibility($l\pi r^2=l_0\pi r_0^2$), we can approximate the maximum engineering longitudinal strain (ε_x) and the maximum engineering transverse strain (ε_y) in terms of the specimen dimensions as

$$\frac{l}{l_0}=\left(\frac{r_0}{r}\right)^2=\frac{1}{(1+\varepsilon_y)^2}=(1-\varepsilon_x)=\lambda \tag{30}$$

Where l_o and r_o are original length and radius, and l and r are the deformed length and radius, respectively. The average strain rate of deformation during the wave propagation may be written as

$$\dot{\epsilon}^*_{avg}=0.5*(1-\lambda_{\max})-\Delta t \tag{31}$$

Where, Δt is the time taken to reach the maximum strain of ($1-\lambda_{max}$). Both λ_{max} and Δt were measured from the high speed images. The factor of 0.5 is assumed for averaging the strain spatially along the length of the sample where the strain varies. For the example shown in Fig. 2, the strain was acquired at $0.5\text{x}10^{-3}$ ms since the acquisition rate of the oscilloscope was 2MegaSamples/s and the data such as wave velocity variation, strain and its derivatives were calculated for a time step (Δt) of $2.72\text{x}10^{-3}$ ms to calculate the right hand side expression of Eq. (29). This value was divided by the body force term to evaluate the effective mass for that particular time t. The average mass over the total time was then calculated as 0.0018kg which was then distributed uniformly over the contact nodes. This exercise required a process where the finite element analysis was run a priori to determine the time step and then calculate the mass on nodes for the next analysis where the analysis for the specimen is to be conducted. For the three tests performed at different input bar velocities shown in Fig. 4, the maximum strain (or stretch), strain rate, and the NH model constant K are given Table 2. A Poisson's ratio of 0.499 has been used in addition to the constant K for all the three cases in the LSDYNA software to simulate the wave generation and pressure conditions such as the radial inertial effect.

Figs. 11 and 12 compare the computed profiles of the gelatin specimen for a strain rate of 600/s at various times during wave propagation with those of the high speed snapshot profiles from the experimental results (Fig. 2). There is a good agreement between the experiments and analysis in terms of the amplitude of the wave crest, wave duration, and the propagation velocity of the wave-front suggesting that the chosen material model on the basis of average strain rate captures the gel behavior reasonably well.

Table 2
Test conditions and Neo-Hookean constant values for the three samples.

Average velocity (m/s)	Maximum strain ($1-\lambda_{max}$)	Average strain rate (1/s)	Neo-Hookean constant K (N/m^2)
3.49	0.42	600	$1.5\text{x}10^4$
2.03	0.28	450	$1.04\text{x}10^4$
1.79	0.19	283	$6.7\text{x}10^3$

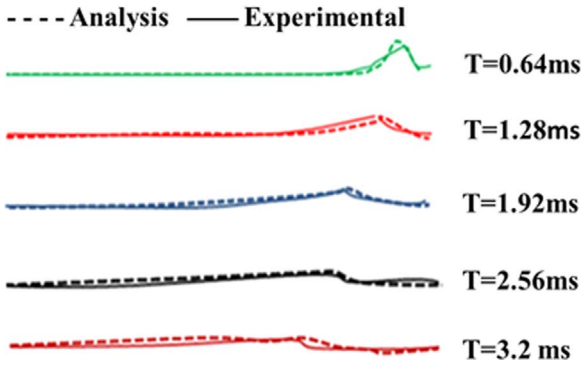

Fig. 11. Comparison of wave profiles in the specimen between the analysis and experiment at different time.

Fig. 13 compares the velocities of the wave-front and wave-crest between the model and experiment for three input bar velocities. It is noted that the wave front velocity (Fig. 13 (a)) in the model and experiment match reasonably well for both the initial phase (where it is aided by the bar impulse) and also later in the steady state regime (where the front slows down). Recall that the wave velocity is a function of stretch in the material, and during the early stage, the stretch (strain) in the material is high due to the immediate influence of the impulse imparted by the incident bar, and the wave front travels at a higher speed. As the influence of the impulse is diminished, the front velocity slows down due to the lower stretch (strain and strain rate) in the material. This is clearly reflected in Fig. 13(a). However, the comparison between the experimental and model crest velocities, shown in Fig. 13(b), is not as good as in Fig. 13(a). During the initial phase, the velocity of propagation of the wave crest from the model is lower than that of the experiments and at a later stage the trend reverses. This result stems from the fact that the strain (stretch) and strain rate are significantly higher in the crest than the wave front, and at higher strain rates the constant K exhibits a highly non-linear response as seen in Fig. 7. The simplified Neo-Hookean model with one constant is unable to capture the complex strain and strain rate dependent response of these materials, especially at large deformations and high strain rates. Interestingly, the crest-velocities at the start (i.e., at t=0 in Fig. 13 (b)) in both the model and experiment match reasonably well, i.e., 7 m/s and 7.4 m/s, respectively, with a difference of only 5.6% which suggest that the chosen Neo-Hookean constant K simulates the initial response well in terms of velocity but later deviates due to the limited flexibility of the model. The non-linear nature of the dependence of the constant on strain rate (see Fig. 7 and Eqs. (5–8)) is more severe at higher strain rates which is responsible for the large deviation in the crest profile and its velocity.

The deviation observed in Fig. 13(b) can be attributed to the strain rate dependence of the material. Since the material constants for the average strain rate was chosen, the response represents an average response. As can be seen in Fig. 13(b), the experimental wave velocity in the initial stages is consistently higher than the analytical wave velocity for all the three experiments. This trend continues up to a certain point and then deviates. This experimental behavior can be intuitively understood in terms of higher strain rates in the initial stages of impulse loading resulting in higher stiffness (and consequently higher wave velocity) and lower strain rates at later stages resulting in a more compliant material (and hence lower wave velocity). On the other hand, the analytical wave velocity variation is only due to prestrain/prestress and not due to change in strain rate because the single Neo-Hookean constant for the average strain rate is chosen for this analysis. This deviation may be alleviated by choosing a complex viscoelastic material model which captures the strain rate dependence well and can be a scope for future work. It would be impossible to

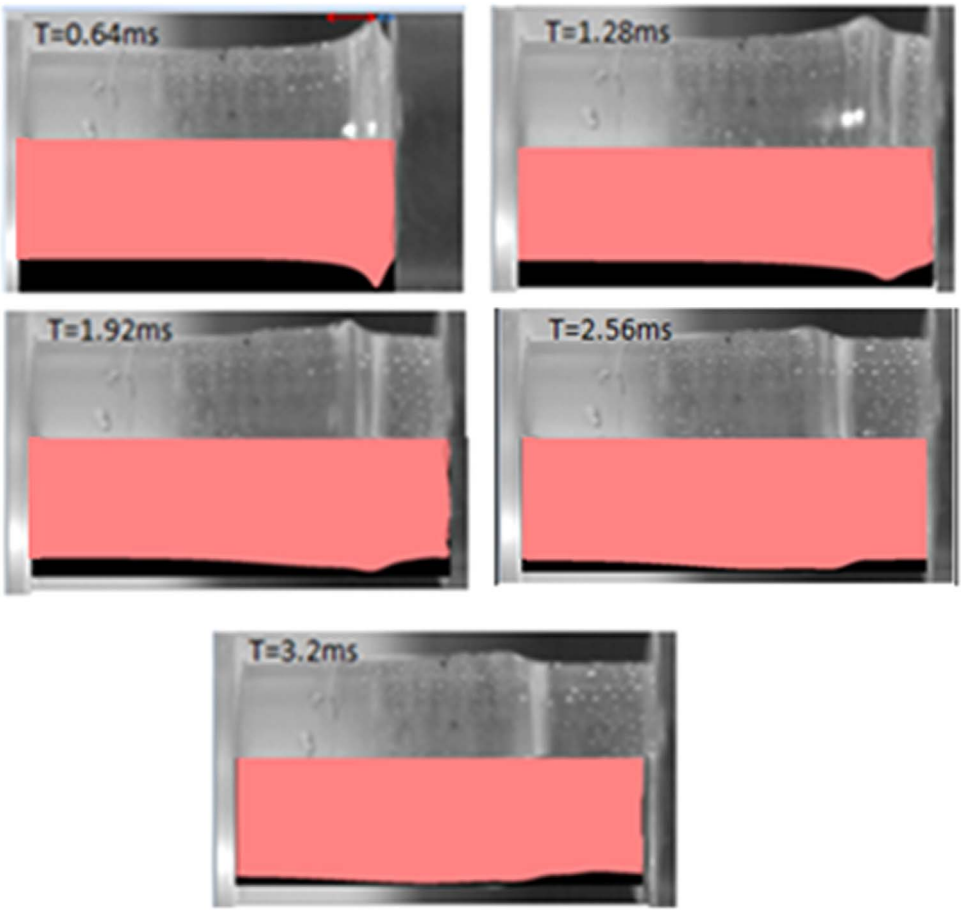

Fig. 12. Comparison between experimental (top half) and finite element simulation (bottom half) for strain rate of 600/s and incident bar impact velocity of 3.49m/s.

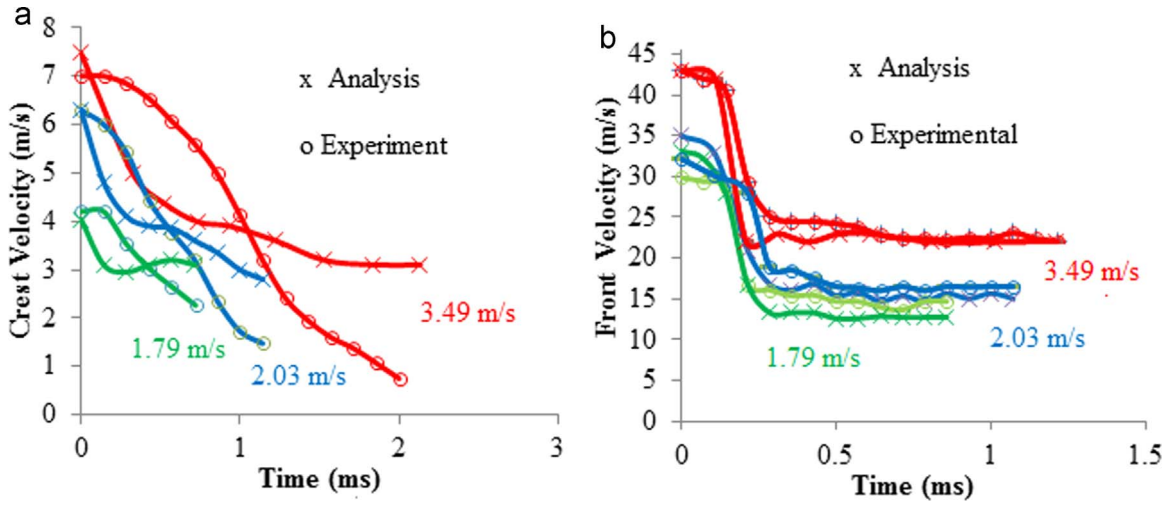

Fig. 13. Comparison between the experimental and model results of (a) wave-front velocity and (b) wave-crest velocity in gelatin.

develop a linear viscoelastic model to encompass the whole range of strain rates (0-6600/s) as nonlinear viscous effects (such as Non-Newtonian behavior) are generally observed in gelatin over larger strain rate range (Subhash et al., 2012) and are responsible for strain rate dependence rather than linear viscous effects. Therefore, a limited linear viscoelastic model over selected range of strain rates which is enough for the modelling of this phenomena can be chosen. It can therefore be concluded that the current Neo-Hookean model captures the overall response in an average sense within the time range of the experiment.

The body force method combined with the Neo-Hookean model based on the strain rate dependence of compression response has been shown to capture the behavior of gelatin during wave propagation reasonably well. Although the average strain rate (600/s) in the wave propagation experiment is considerably lower than the maximum strain rate (6600/s) utilized in the Hopkinson pressure bar experiments, such a study was warranted to obtain the complete strain rate dependence of the model constants as shown in Fig. 7. While the two constant Mooney-Rivlin model has a greater flexibility, by defining an equivalent Neo Hookean model constant allowed for simpler analysis

that captured the apparent dispersion and attenuation of the wave in gelatin specimen effectively.

6. Conclusion

Wave propagation experiments on cylindrical ballistic gelatin samples revealed that the velocities of wave-crest and wave-front decrease with time and there is a simultaneous attenuation and dispersion of the wave crest. Analytical expression for the dilatational wave velocity in gelatine is derived using Mooney-Rivlin and Neo-Hookean material models in terms of the stretch in gelatine. The decrease in the wave velocity with attenuation of the transverse displacement (the crest) is explained through the dependence of the longitudinal wave velocity on the stretch of a hyperelastic material. It is found that the initial wave velocity depends on the constants in both the models and the sum of the Mooney-Rivlin constants is proportional to the initial dilatational wave velocity.

The constitutive response of ballistic gelatin as a function of strain-rate was modelled using Mooney-Rivlin and Neo-Hookean material models and a cubic relationship between the logarithm of the sum of the Mooney-Rivlin constants and strain rate was observed. The equivalent Neo-Hookean material which has the same initial wave velocity as that of the Mooney-Rivlin model was defined with the Neo-Hookean constant being proportional to the sum of the Mooney-Rivlin constants. It was found that the Neo-Hookean model stress-strain curves match the Mooney-Rivlin model well within the true compressive strain range up to 0.58.

The dynamics of the interaction between the incident bar and the ballistic gelatin was modelled using lumped masses, based on the average body force transferred by the incident bar, at the nodes of the ballistic gelatin in LS-DYNA software. This method yielded good correlation between the model and experimental result for the wave propagation.

Acknowledgements

This work was supported by the National Science Foundation Award No.1634188. The first author from the National Aerospace Laboratories, Bangalore, India, thanks Director General, Council of Scientific and Industrial Research, New Delhi and Director, National Aerospace Laboratories for deputing the author to University of Florida- USA for Post-Doctoral Research work under Raman Research Fellowship. The author especially wants to thank Dr Satish Chandra, Head, Structural Technologies Division NAL, Bangalore, for his constant support and encouragement for pursuing the Post-Doctoral work at University of Florida.

References

Airoldi, A., Cacchione, B., 2006. Modelling of impact forces and pressures in Lagrangian bird strike analyse. Int. J. Impact. Eng. 32, 1651–1677.
Appleby Thomas, G.J., Hazell, P.J., Wilgeroth, J.M., Shepherd, C.J., Wood, D.C., Roberts, A., 2011. On the dynamic behavior of three readily available soft tissue simulants. J. Appl. Phys. 109 (084701), 1–6.
Burridge, R., Knopoff, L., 1964. Body force equivalents for seismic dislocations. B. Seismol. Soc. Am. 54 (6), 1875–1888.
Chen, W., Zhang, B., Forrestal, M.J., 1999. A split Hopkinson bar technique for low-impedance materials. Exp. Mech. 39, 81–85.
Cronin, D.S., Falzon, C., 2009. Dynamic characterization and simulation of ballistic gelatin. Proceedings of the SEM Annual Conference, Society for Experimental Mechanics Inc., Albuquerque New Mexico USA.
Cronin, D.S., Falzon, C., 2011. Characterization of 10% ballistic gelatin to evaluate temperature, aging and strain rate effects. Exp. Mech. 51, 1197–1206.
Heimbs, S., 2011. Computational methods for bird strike simulations: a review. Comput. Struct. 89, 2093–2112.
Johnson, A.F., Holzapfel, M., 2003. Modelling soft body impact on composite structures.. Comput. Struct. 61, 103–113.
Jussila, J., 2004. Preparing ballistic gelatine—review and proposal for a standard method. Forensic Sci. Int. 141, 91–98.
Jussila, J., 2005. Wound ballistic simulation: assessment of the legitimacy of law enforcement firearms ammunition by means of wound ballistic simulation (Thesis). Second Department of Surgery, University of Helsinki, Finland.
Kobayashi, H., Vanderby1, R., 2005. New strain energy function for acoustoelastic analysis of dilatational waves in nearly incompressible hyper-elastic materials. J. Appl. Mech.-T. ASME. 72, 843–851.
Kwon, J., Subhash, G., 2010. Compressive strain rate sensitivity of ballistic gelatin. J. Biomech. 43, 420–425.
Liu, L., Jia, Z., Ma, X.L., Fan, Y.R., 2013. Analytical and experimental studies on the strain rate effects in penetration of 10wt % ballistic gelatin. J. Phys. Conf. Ser. 451 (012035), 1–7.
Liu, Q., Subhash, G., Evensen, H., 2005. Behavior of a novel iterative deconvolution algorithm for system identification. J. Vib. Control 11, 985–1003.
Liu, Q., Subhash, G., 2006. Characterization of viscoelastic properties of polymer bar using iterative deconvolution kin the time domain. Mech. Mater. 38, 1105–1117.
LSDYNA Software Version, smps R8.0.0
Naarayan, S.S., Dhayanidhi, J., Nagarajappa, B., Yathish, V., Chandra, S., 2015. Behavior of organic gelatine/phenolic micro balloon composite under compressive loading, static and low velocity impact, Indian. J. Eng. Mater. S 22, 618–630.
Nishida, E., 2010. Distinguishing Inertia Effects from the Intrinsic mechanical behavior of soft materials at high strain rates by Kolsky bar experiment (M.S. Thesis). Purdue University, USA.
Nishida, E and Chen W.W., 2010. “Inertia effects in the impact response of soft materials”, in Proceedings IMPLAST 2010 Conference, publ. Bethel, CT, Society for Experimental Mechanics
Ravikumar, N., Noble, C., Cramphorn, E., Zeike, A., Taylor, A., 2015. Constitutive model for ballistic gelatin at surgical strain rates. J. Mech. Behav. Biomed. Mater. 47, 87–94.
Richler, D., Rittel, D., 2014. On the testing of the dynamic mechanical properties of soft gelatins. Exp. Mech. 54, 805–815.
Salisbury, C.P., Cronin, D.S., 2009. Mechanical properties of ballistic gelatin at high deformation rates. Exp. Mech. 49, 829–840.
Shepherd, C. J., Appleby-Thomas, G. J., Hazell, P. J. Allsop, D. F., 2009. The Dynamic Behavior of Ballistic Gelatin. Proceedings of the American Physical Society Topical Group on Shock Compression of Condensed Matter AIP, Melville, New York USA.
Song, B., Chen, W., 2004. Dynamic stress equilibration in split Hopkinson pressure bar tests on soft materials. Exp. Mech. 44, 300–312.
Song, B., Chen, W., 2005. Split Hopkinson pressure bar techniques for characterizing soft materials. Lat. Am. J. Solids Struct., 113–152.
Subhash, G., Kwon, J., Mei, R., Moore, D.F., 2012. Non-newtonian behavior of ballistic gelatin at high shear rates. Exp. Mech. 52, 551–560.
Subhash, G., Ravichandran, G., 2000. Split Hopkinson pressure bar testing of ceramics. ASM Handb., Mech. Test. Eval. 8, 497–504.
Toyoda, Y., Gupta, Y.M., 2014. Shockless and shock wave compression of ballistic gel to 1.3 GPa. J. Appl. Phys. 116 (153512), 1–8.
Timoshenko, S.P., Goodier, J.N., 1970. Theory of Elasticity. Mc Graw-Hill International Editions, Singapore.
Treloar, L.R.G., 1975. The Physics of Rubber Elasticity. Clarendon Press, Oxford, UK.
Warren, T.L., Forrestal, M.J., 2010. Comments on the effect of radial inertia in the kolsky bar test for an incompressible material. Exp. Mech. 50, 1253–1255.
Wen, Y., Xu, C., Wang, H., Chen, A., Batra, R.C., 2013. Impact of steel spheres on ballistic gelatin at moderate velocities. Int. J. Impact. Eng. 62, 142–151.
Wightman, G., Beard, J., Allison, R., 2010. An investigation into the behaviour of air rifle pellets in ballistic gel and their interaction with bone. Forensic. Sci. Int 200, 41–49.
Wilbeck, J.S., James, R.L., 1981. The development of a substitute bird model. J. Eng. Power. 103, 725–730.